Organic ElectroOptic Mach–Zehnder Modulators: From PhysicsBased to SystemLevel Modeling

physica status solidi a
www.pss-a.com

Organic Electro-Optic Mach–Zehnder Modulators: From Physics-Based to System-Level Modeling

*Alberto Tibaldi, Mohammadamin Ghomashi, Francesco Bertazzi, Michele Goano, Marco Vallone, and Giovanni Ghione**

Herein, an overview on the physics-based and system-oriented modeling of organic electro-optic Mach–Zehnder modulators for optical communication systems is presented. State-of-the-art solutions in electro-optic organic materials and modulator designs are reviewed, with particular stress on silicon organic hybrid (SOH) and plasmonic organic hybrid (POH) solutions. Then, the physics-based simulation of concentrated and traveling-wave modulators is discussed both through 3D optical simulations and a combination of 2D and 3D models, where the modulator is partitioned into convenient subdomains. Neural network behavioral models are finally discussed and case studies are proposed on the physics-based and system-level simulation of SOH and POH Mach–Zehnder modulators.

1. Introduction

The evolution of optical communication systems has led, over the years, to a constant request for increased data throughput both in short-range, datacenter-level interconnects and in long-range links. High-speed modulation of the light source (typically a laser) is the fundamental enabling step for any high-data-rate optical transmission. Modulation can be performed either directly, by changing the source instantaneous bias current, or indirectly, by introducing an external modulator.

Two main solutions are currently available for external amplitude modulation, which can be classified according to the physical operation principle: the electro-optic modulator (EOM) and the electroabsorption modulator (EAM).[1,2] While EAMs are based on the modulation of the material absorption (or, equivalently, of the imaginary part of the complex refractive index) by an applied electric field, in EOMs the amplitude modulation is obtained by properly exploiting the phase modulation of the optical signal caused by the modulation of the (real) refractive index induced by an applied electric field or injected current. EOMs can be implemented according to several solutions, the most widespread ones being the Mach–Zehnder (MZ) and the ring modulators. EOMs have a broader application field than EAMs, as the implementation of complex modulation formats typically require EOMs, see for example, the in-phase and quadrature (IQ) modulators consisting of two MZ EOMs. MZ modulators (MZMs), on whose modeling we will concentrate in the present article, can be further classified according to the material platform exploited, which can be based on III–V semiconductors (GaAs and InP[3]), perovskites (such as lithium niobate, $LiNbO_3$[4]), and, last but not least, silicon.[5] (Recently, also III-N semiconductors have been proposed as EOM candidates.[6]) While III–V semiconductors and perovskites exhibit the linear (Pockels) EO effect, silicon features only the much weaker quadratic (Kerr) effect. Si-based integrated photonics (SiPh) has, however, seen an impressive development during the past few years, as it offers the possibility to realize, with processes compatible with complementary metal-oxide semiconductor (CMOS-compatible) integrated circuits, wideband photonic and optoelectronic elements directly integrable with digital or analog electronic subsystems.[7,8] For this reason, several strategies have been proposed to integrate EO modulators into SiPh platforms, based either on the heterogeneous integration of III–V modulators, or on the plasma effect in Si p–n or metal–insulator–semiconductor (MIS) junctions, or, finally, on EO films deposited on Si.[9]

In the present work, we will focus on the modeling and simulation (from the physical to the system level) of MZMs based on organic EO (OEO) materials, in particular on the silicon organic hybrid (SOH) and plasmonic organic hybrid (POH) solutions, which pose interesting simulation challenges. To this aim, we will provide first a review on EO organic materials (Section 2), followed by an overview of discrete, SOH, and POH modulator solutions (Section 3). Section 4 is devoted to a discussion on simulation techniques, ranging from the physical-level to the system-oriented, behavioral level. The physics-based simulation of

A. Tibaldi, M. Ghomashi, F. Bertazzi, M. Goano, M. Vallone, G. Ghione
Dipartimento di Elettronica e Telecomunicazioni
Politecnico di Torino
corso Duca degli Abruzzi 24, 10129 Torino, Italy
E-mail: giovanni.ghione@polito.it

A. Tibaldi, F. Bertazzi, M. Goano
IEIIT-CNR c/o Politecnico di Torino
corso Duca degli Abruzzi 24, 10129 Torino, Italy

The ORCID identification number(s) for the author(s) of this article can be found under https://doi.org/10.1002/pssa.202100390.

DOI: 10.1002/pssa.202100390

organic MZMs in principle requires 3D multiphysics simulation tools, which are often impossible to exploit due to the sheer complexity of the problem. To alleviate the computational burden of this "all-in-one" (AiO) approach (that is practically feasible only for POH MZMs), we propose alternative, accurate, but computationally efficient partitioning strategies (a "divide-and-conquer" [DaC] approach) based on the mixed use of 3D and 2D models. Section 5 is devoted to a number of case studies concerning the physics-based simulation of SOH and POH MZMs and their system-level behavioral modeling through a neural network approach. Some conclusions are finally drawn in Section 6.

2. Organic Electro-Optic Materials

Organic materials have been the object of intensive study since the early 1970s for their electrical and optical properties. In particular, π-conjugate polymers (like, e.g., polyacetylene) were demonstrated to behave as conductors or semiconductors and support optical transitions in the near-infrared (NIR) and visible ranges.[10] In addition, some large organic molecules formed by an acceptor- and a donor-like functional group connected by a conducting π-conjugated bridge (so-called "chromophores"; due to their activity in the visible range, chromophores appear as colored, from which the name, meaning "color carriers", is derived) were also shown to exhibit strong nonlinear polarizability, making them interesting optically nonlinear—and therefore EO—materials. Such molecules can be either incorporated into a polymer matrix (see the study by Rau et al.[11] for a recent review) or be part of an organic crystal (see the study by Chen et al.,[12] and the study by Jazbinsek et al.[13]). Thanks to the technological opportunities offered by EO organic materials, such as low-temperature processing, a new wave of interest was brought about by the introduction of these materials within the framework of a Si photonic platform, either under the form of SOH modulators or, later, in connection with the POH approach.

The EO properties of materials can be more generally viewed as a particular case of the material dielectric nonlinearity, that is, the fact that the electric displacement field $\underline{\mathcal{D}}$ is a nonlinear function of the applied electric field $\underline{\mathcal{E}}$. The instantaneous electric displacement can be expressed in terms of the electrical polarization $\underline{\mathcal{P}}$ as

$$\underline{\mathcal{D}}(t) = \varepsilon_0 \underline{\mathcal{E}}(t) + \underline{\mathcal{P}}(t) \tag{1}$$

where ε_0 is the free space permittivity and the polarization expresses the response of the material to the applied field. Neglecting memory effects for simplicity of notation (accounting for memory effects amounts to expressing the frequency-domain components of the polarization as a Volterra series of the components of the applied electric field;[14] for the second-order nonlinear polarization, an explicit expression can be found in ref. [15], Equation 1.3.12), we can expand the components of $\underline{\mathcal{P}}(t)$ in a power series of the components of the applied field

$$\begin{aligned}\mathcal{P}_i(t) = {} & \varepsilon_0 \sum_j \chi^{(1)}_{ij} \mathcal{E}_j(t) + \varepsilon_0 \sum_{jk} \chi^{(2)}_{ijk} \mathcal{E}_j(t)\mathcal{E}_k(t) + \\ & + \varepsilon_0 \sum_{jkl} \chi^{(3)}_{ijkl} \mathcal{E}_j(t)\mathcal{E}_k(t)\mathcal{E}_l(t) + \ldots\end{aligned} \tag{2}$$

where the coefficients $\chi^{(n)}$ are the n-th order susceptibilities of the medium, in general a tensor of rank $n+1$. According to a different, microscopic approach (see ref. [15], Chapter 5), the "molecular" polarization $\underline{p}$ of a material can be similarly expressed as a power series in terms of the component p_i, obtaining the same format as in Equation (2) but with coefficients (up to third order) α_{ij}, β_{ijk}, and γ_{ijkl}. In particular, the second-order coefficient β is the "hyperpolarizability tensor," expressing the second-order intrinsic properties of a single optically nonlinear (nonlinear optical, NLO) organic molecule. The macroscopic second-order susceptibility $\chi^{(2)}$ is instead the result of both the properties of the NLO organic molecule and its dispersion in a host medium.

The first-order susceptibility $\chi^{(1)}$ is related to the linear material response, that is, the absolute permittivity of the material $\varepsilon_{ij} = \varepsilon_0 + \varepsilon_0 \chi^{(1)}_{ij}$, whereas the other terms describe the medium nonlinearity and are the causes of phenomena such as the generation of harmonics, frequency mixing, and the EO effect. The modulation of the dielectric permittivity caused by the EO effect is due to the material excitation from a total electric field being the sum of an optical field $\underline{\mathcal{E}}_o(t)$ and a DC or radiofrequency (RF) field $\underline{\mathcal{E}}_{RF}(t)$. In particular, the second- and third-order terms $\chi^{(2)}$ and $\chi^{(3)}$ are related to the linear (Pockels) and quadratic (Kerr) EO effects, respectively. The Pockels effect, which implies a linear variation of the material refractive index around $\underline{\mathcal{E}}_{RF} = 0$, vanishes in centrosymmetric materials, as is the case for crystals and for general molecules having a central inversion symmetry, see ref. [15], Section 1.5.10. Organic EO materials typically exhibit the Pockels effect according to which the variation of the dielectric permittivity tensor ε can be expressed (always dropping for simplicity of notation memory effects, i.e., frequency dispersion) as

$$\Delta\varepsilon_{ij} = 2\varepsilon_0 \sum_k \chi^{(2)}_{ijk} \mathcal{E}_{RFk}(t) \tag{3}$$

where we have applied the so-called Kleinmann's symmetry condition ($\chi^{(2)}_{ijk} = \chi^{(2)}_{ikj}$) (see ref. [15], Section 1.5.5). The linear EO effect is more often expressed in terms of the second-order EO tensor $\mathbf{r}$ with components r_{ijk} as

$$\varepsilon_0 \Delta\varepsilon^{-1} = \mathbf{r} \cdot \underline{\mathcal{E}} \tag{4}$$

that is, by components, taking into account that for any matrix $\mathbf{K}$, and in the limit of small variations, one has $\Delta\mathbf{K} = -\mathbf{K} \cdot \Delta\mathbf{K}^{-1} \cdot \mathbf{K}$

$$\begin{aligned}\Delta\varepsilon_{lm} &= -\tfrac{1}{\varepsilon_0} \sum_{ijk} (\varepsilon)_{li} r_{ijk} \mathcal{E}_{RFk} (\varepsilon)_{jm} \\ &= -\tfrac{1}{\varepsilon_0} \sum_k \left[\sum_{ij} (\varepsilon)_{li} r_{ijk} (\varepsilon)_{jm} \right] \mathcal{E}_{RFk}\end{aligned} \tag{5}$$

Assuming that the permittivity matrix can be expressed along the principal axes as $\varepsilon = \varepsilon_0 \mathrm{diag}(n^2_{ii})$, we also have

$$\Delta\varepsilon_{ij} = -\varepsilon_0 \sum_k n_{ii}^2 n_{jj}^2 r_{ijk} \mathcal{E}_{\mathrm{RF}k} = 2\varepsilon_0 \sum_k \chi_{ijk}^{(2)} \mathcal{E}_{\mathrm{RF}k}(t) \tag{6}$$

Thus, the relationship between second-order susceptibility and second-order EO tensor is (see, e.g., ref. [16], Equations 12.1-1, 12.2-14)

$$r_{ijk} = -2\chi_{ijk}^{(2)} / n_{ii}^2 n_{jj}^2 \tag{7}$$

Frequency dispersion arising from memory effects is generally present, both for the linear and for the nonlinear susceptibilities,[15] also in OEO materials. A theoretical analysis based on a classical anharmonic oscillator model, see ref. [15], Section 1.4, shows that the frequency behavior of the linear and second-order susceptibilities is strictly related. In fact, the linear susceptibility dispersion can be modeled as the superposition of second-order-damped resonant responses

$$\chi^{(1)}(\omega_j) = \sum_k \chi_k^{(1)}(\omega_j) = \sum_k \frac{K_k}{D_k(\omega_j)} \tag{8}$$

where K_k is a constant, $D_k(\omega_j) = \omega_{0k}^2 - \omega_j^2 + 2\mathrm{j}\omega_j\xi_k$ and ω_{0k} and ξ_k are resonant frequencies and damping factors, respectively. The second-order susceptibility contributions in the presence of an optical plus RF excitation at frequencies ω_o and ω_{RF} can be expressed as

$$\begin{aligned}\chi_k^{(2)}(\omega_o \pm \omega_{\mathrm{RF}}) &= H_k \chi_k^{(1)}(\omega_o \pm \omega_{\mathrm{RF}}) \chi_k^{(1)}(\omega_o) \chi_k^{(1)}(\pm\omega_{\mathrm{RF}}) \\ &\approx H_k [\chi_k^{(1)}(\omega_o)]^2 \chi_k^{(1)}(\pm\omega_{\mathrm{RF}})\end{aligned} \tag{9}$$

where H_k is a constant, see ref. [15], Equations 1.4.25 and 1.4.27. For an optical source in the NIR range, the second-order nonlinear susceptibility therefore mainly depends on the linear susceptibility dispersion from the DC to RF range. While some organic crystals may exhibit low-frequency dispersion, see ref. [10], Chapter 11, the refractive index of polymers is expected to show little dispersion over frequency, since in organic materials, the linear and nonlinear susceptibilities are related to the extremely fast electronic response. From a modeling standpoint, this amounts to characterizing the r_{ijk} elements of the EO tensor as independent from the RF excitation frequency.

Research on OEO materials has proposed a quite impressive variety of crystals and chromophore-loaded polymers that outperform traditional EO materials such as $LiNbO_3$. The application of a static or RF electric field to the chromophore causes a distortion of the microscopic potential, quantum-mechanically leading to a variation of the energy levels between which optical transitions occur. This in turn leads to a modulation of the absorption profile and, from the Kramers–Kronig relationships, a variation of the real refractive index. To achieve high EO activity, dipolar NLO chromophores with high molecular hyperpolarizability β and good thermal stability have to be designed (through ab initio simulation techniques and computational chemistry tools) and synthesized, see the study by Xu et al.[17] and references therein. If the chromophore dipole moments have a random orientation after dispersion in a polymer matrix, the average influence of the RF electric field will be zero. This implies that the chromophores should be oriented, for example, through the application of a strong static electric field, to achieve a nonzero global effect. This orientation procedure can be conducted through several techniques, generally termed as "poling," such as the static field poling, the photoassisted poling, and the all-optical poling (see the study by Kajzar et al.,[18] Section 4). Poling enables to achieve, within the same polymer sample, regions with opposite orientation, thus leading to $\pm\Delta n$ variations and therefore opposite phase shifts by application of a field having the same direction; this is an additional degree of freedom in the design of push–pull MZMs. For device applications, chromophores should possess low optical loss, long-term stability of polar order following poling, and good solubility and compatibility with the polymer matrix. Note that the resulting EO effect in a chromophore-loaded polymer is not only related to the chromophore hyperpolarizability β but also to its number density; however, r exhibits a non-monotonic behavior versus the chromophore number density, which can be attributed to interaction effects between molecules (see the study by Dalton,[19] Section 4.1).

The literature presents a very large number of NLO material solutions; although chromophore-loaded polymers with the EO coefficient along the poling direction r_{33} (in the contracted index notation) well in excess of 200 pm V^{-1} have been developed, see, for example, the study by Heni et al.,[20] Table I, and references therein, record values obtained in bulk tend to significantly decrease when the material is deposited and poled in slots, particularly for submicrometer slot widths (the study by Heni et al.,[20] Figure 2), leading to record effective device-level values of $r_{33} \approx 200$ pm V^{-1}. Organic EO crystals such as diethylaminosulfur trifluoride (DAST) exhibit in contrast a lower r_{33} (48 pm V^{-1} at 1535 nm,[13]). From the standpoint of EO modulator applications, EO polymers are favored by the flexibility in deposition techniques, in particular for SOH and POH modulator solutions.

From a system standpoint, to compare the potential of EO polymers in modulator applications with III–V materials (e.g., GaAs) and $LiNbO_3$, a figure of merit is sometimes used,[19] defined as

$$\mathrm{FOM} = n_o^3 r / n_{\mathrm{RF}}^2 \tag{10}$$

where n_{RF} is the RF effective index, n_o is the optical index, and r is in pm V^{-1}. To have a fair comparison, let us suppose, for instance, consider a conventional coplanar waveguide electrode set with the same geometry; for $LiNbO_3$, we have $n_{\mathrm{RF}} \approx 4$, $n_o \approx 2.2$, and $r \approx 31$ pm/V with $\mathrm{FOM}_{\mathrm{LiNbO}} \approx 21$; for GaAs, $n_{\mathrm{RF}} \approx 2.6$, $n_o \approx 3.5$, and $r \approx 1.5$ pm/V with $\mathrm{FOM}_{\mathrm{GaAs}} \approx 9$; for EO polymers, $n_{\mathrm{RF}} \approx 1.6$, $n_o \approx 1.6$, and $r \approx 100$ pm/V with $\mathrm{FOM}_{\mathrm{poly}} \approx 164$. The variation of the refractive index with the RF field (see, e.g., ref. [1], Equation 6.8)

$$\Delta n_o = -n_o^3 r_{33} \mathcal{E}_3 / 2 \tag{11}$$

implies that the on−off voltage scales as the inverse of $n_o^3 r_{33}$ (see e.g. ref. [1], Equation 6.16), giving the EO polymer ≈ 25% advantage over $LiNbO_3$ and a more than 6 times advantage over GaAs. As shown in the study by Dalton,[19] Table 2, EO polymers also exhibit similar optical and RF refractive indexes, thus allowing for better synchronous coupling between the optical and microwave signal in traveling-wave (TW) modulators, with optical losses comparable with $LiNbO_3$.

From a modeling standpoint, poled EO organic materials could exhibit an anisotropic behavior, as the only significant element of the EO tensor is the one oriented along the direction of the poling field. If the material is poled exploiting the same electrode setting as the one exploited in the modulator (but in DC conditions), the resulting material model should allow for position-dependent anisotropy. A discussion on the impact of this issue in the modeling of POH modulators is presented in Section 5.2.

3. MZ Organic Modulators

Polymer-based modulators have been receiving constant interest in the literature since the early 90s. Research initially focused on stand-alone devices, alternative to discrete $LiNbO_3$ MZMs. Most examples exploit a microstrip layout, for example, the 20 GHz dual-drive MZM in the study by Girton et al.,[21], with $V_\pi = 9$ V, uniform poling, and transverse magnetic (TM) polarization, somewhat similar to z-cut $LiNbO_3$ modulators; 100 GHz bandwidth was demonstrated in the study by Chen et al.[22] A push–pull poling solution allowed to reduce V_π to 8 V, as shown in the study by Wang et al.[23] After the 1990−2000 development phase, the technology seemed to be ready for market deployment as a competitor to $LiNbO_3$ modulators, see the devices developed by Pacific Wave Industries (around 2002) and GigOptix (around 2010).[24,25] Modulation bandwidths ranged from 30 to 65 GHz with on–off voltages between 3 and 6 V and electrical and optical insertion loss comparable with $LiNbO_3$ modulators. Long-term stability problems affecting organic MZMs are often claimed to have hindered their practical use. However, a comprehensive analysis of the (2010) state of the art seems to suggest that the long-term stability of some EO polymers is indeed satisfactory.[26] Also, EO organic modulators exploiting polymers having glass transition temperatures up to 194 °C exhibit constant on–off voltage at 105 °C for ≈2000 h and stable frequency response up to 40 GHz at 130 °C.[27] Research on conventional, discrete MZMs after 2000 continued with material and layout improvements and aimed at reducing the driving voltage, see the solution (2010) in the study by Michel et al.[28] with a double-loop structure and $V_\pi = 2.6$ V at 1550 nm and 3 GHz bandwidth. Further examples are in other studies[29–31] (with a record $V_\pi = 0.9$ V and 23 GHz modulation bandwidth).

As discussed in Section 2, Si exhibits zero Pockels effect due to crystal symmetry, thus requiring Si-based modulators to operate on the basis of the so-called plasma effect. SOH modulators have been proposed as a solution able to integrate high-performance EO organic materials into a Si platform. In the SOH approach, passive components, such as waveguides, couplers, and filters, are fabricated in silicon. The high refractive index of silicon ($n \approx 3.5$) allows for strongly guided optical waveguides. The nonlinear (Pockels or Kerr) optical functionality, however, is taken over by suitable EO organic materials. A typical coplanar electrode setup for SOH modulators is shown in **Figure 1**.[32] Slot widths are around 100 nm, whereas the Si ribs are moderately doped not to increase optical losses. As the EO polymer refractive index is lower than the Si index, the optical field is not strongly (laterally) confined to the slot, whereas the RF field is, leading to an only partial overlap.

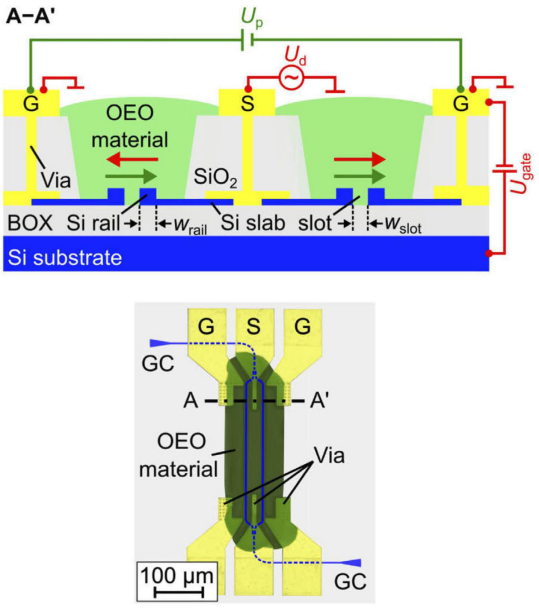

Figure 1. Example of implementation of SOH MZM. Above: Cross section with slot Si-doped rib electrodes supporting the RF field in the OEO material operating as the optical waveguide. Below: MZ layout. Adapted with permission.[32] Copyright 2020, The Optical Society.

A comparative analysis in the study by Leuthold et al.,[33] Table 3.4, shows that millimeter-long slot modulators, with driving voltages of the order of 1 V, exhibit (in concentrated or TW configurations) cutoff frequencies well in excess of 100 GHz. Relevant design examples proposed during the past decade can be found in various studies.[34–39] In the study by Wolf et al.,[39] Figure 5, a performance comparison is presented, showing the drive voltage and V_π versus the modulator speed for different modulator technologies. In particular, it is shown how SOH MZMs operating at 100 Gbps have a $V_\pi \approx 0.9$ V against the InP counterpart $V_\pi \approx 2$ V. As a recent example of state-of-the art SOH MZMs in the study by Kieninger et al.,[32] a 200 Gbps push–pull modulator is presented, achieving 0.41 V mm $V_\pi L$ and $V_\pi \approx 1.5$ V for 280 µm-long phase shifters (PSs), see Figure 1. The EO polymer exhibits $r_{33} \approx 300\ \mathrm{pm\ V^{-1}}$ with a slot width $w = 120$ nm that increases to $390\ \mathrm{pm\ V^{-1}}$ for $w = 190$ nm. Another important parameter in comparing the performances of the EO modulator is the $\alpha V_\pi L$ product, where αL is the total optical insertion loss of the modulator. Following the discussion in the study by Kieninger et al.,[32] Section 1, representative values for $\alpha V_\pi L$ ($V_\pi L$) are 0.5 V dB (20 V mm) for $LiNbO_3$ modulators, 0.9 V dB (6 V mm) for InP modulators, 5.8 V dB (4.6 V mm) for depletion-mode Si modulators, and 1 V dB (0.41 V mm) for the SOH modulator.[32] $LiNbO_3$ exhibits the lowest specific optical losses but requires long, TW modulators to achieve low-enough V_π with bandwidths of the order of 40 GHz. InP is more favorable but still often requires a distributed slow-wave structure that is complex to implement and increases the length of the optical path introducing EO inactive sections. Plasma effect-based Si modulators are penalized by high optical losses and may need again distributed approaches to obtain bandwidths in excess of 10 GHz. The SOH approach

finally appears to be able to achieve the best compromise, with a length bandwidth product of around 30 GHz mm in a concentrated implementation. Notice, however, that the slot width required to obtain such a low $V_\pi L$ ultimately is of the order of 100 nm.

During the past few years, several optoelectronic functionalities have been implemented through plasmonic waveguides.[42] Surface plasmon polaritons (SPPs) are surface waves carried by the interface between a material of negative permittivity and one of positive permittivity. Due to this surface-wave feature, SPPs can exist independent from the size of the guiding system versus the operating wavelength, that is, they are not diffraction limited. Despite such promising properties, the use of plasmonic waveguides in photonic integrated circuits is fraught with difficulties: from a technological standpoint, most typical integrated circuit (IC) metals (like Al) have unsatisfactory performances and must be replaced by metals like Au. Even with the best metals, optical losses are large (of the order of 0.2–0.8 dB μm^{-1}), and therefore long components are hardly feasible. EO modulators, however, may be a field where the potential of plasmonics can be conveniently exploited, as the nanometer cross section of plasmonic waveguides, together with the excellent overlap between the optical and RF fields, allow large-index variations to be obtained also with moderate applied voltages, thus yielding significant phase modulations over an interaction length of few micrometers, not incompatible with the requirements on optical insertion loss. Moreover, the use of EO polymers in POH modulators makes them amenable to integration into a SiPh platform. During the past few years, POH MZMs have been proposed by some research groups, with impressive performance in terms of modulation bandwidth but, for the moment, with quite large on-state optical insertion losses. Notice that the insertion loss penalty is also connected with the need to couple a photonic waveguide with the plasmonic medium, where modulation is conducted. From the optical insertion loss standpoint, a possible alternative is represented by the (optically narrowband) plasmonic ring modulators.[43]

In the past decade, research on plasmonic modulators investigated a number of EOM and EAM solutions, exploiting organic or inorganic EO materials (like ITO and ferroelectric materials), see various studies.[44–50] A research line on organic plasmonic EO modulators leading to experimental realizations was initiated in 2014 through the cooperation of a number of research groups (initially from the Karlsruhe Institute of Technology—KIT, ETH Zürich, IMEC, and GigOptix) and continued through the following years. In the study by Melikyan et al.,[51] Au plasmonic POH phase modulator was presented based on an EO polymer with maximum estimated EO coefficient of 70 pm V^{-1} after poling, integrated into an SOI platform with a 2 μm SiO_2 thick layer; the modulator length was around 30 μm. The structure was experimentally demonstrated showing binary phase-shift keying (BPSK) modulation up to 40 Gbps.

Starting from 2015, a number of MZM POH designs were proposed, realized, and characterized, exploiting coplanar electrode configurations coupled to slot plasmonic waveguides. Designs vary not only for the slot width and metal thickness, but also for the spacing between plasmonic slots (that can be as low as to introduce coupling between plasmonic modes) and for the design of photonic–plasmonic transitions and splitter/combiner sections. A first design was presented in the study by Melikyan et al.[52] including two parallel, uncoupled phase modulators with 150 nm slots in a ground–signal–ground configuration. The splitter/combiner section was external and a Si photonic waveguide taper with a 450 × 220 nm^2 cross section was used as a plasmonic launcher; the phase modulation length ranged from 19 to 39 μm, with a $V_\pi L$ product of 450 V μm (29 μm device); the optical insertion loss of the PS ranged from 13 to 20 dB, depending on the length; the modulation bandwidth was in excess of 60 GHz.

A more compact layout was presented in the study by Haffner et al.[53] (see **Figure 2**, above), with >70 GHz modulation bandwidth and 10 μm total length (with a PS length of 5 μm); the $V_\pi L$ product was as small as 60 V μm. A very compact design was exploited for the splitter/combiner sections that integrate a photonic waveguide taper operating both as a launcher and as a splitter/combiner, with an insertion loss of around 3 dB. The on–off voltage was close to 10 V and the extinction ratio was estimated from simulations to be around 26 dB, see the study by Haffner et al.,[54] Figure S1c, Supporting Information. The modulator optical insertion loss was 8 ± 1 dB, resulting from the couplers loss and the plasmonic loss of 0.4 dB μm^{-1}. As the 70 GHz bandwidth was mainly limited by the input pad capacitance,

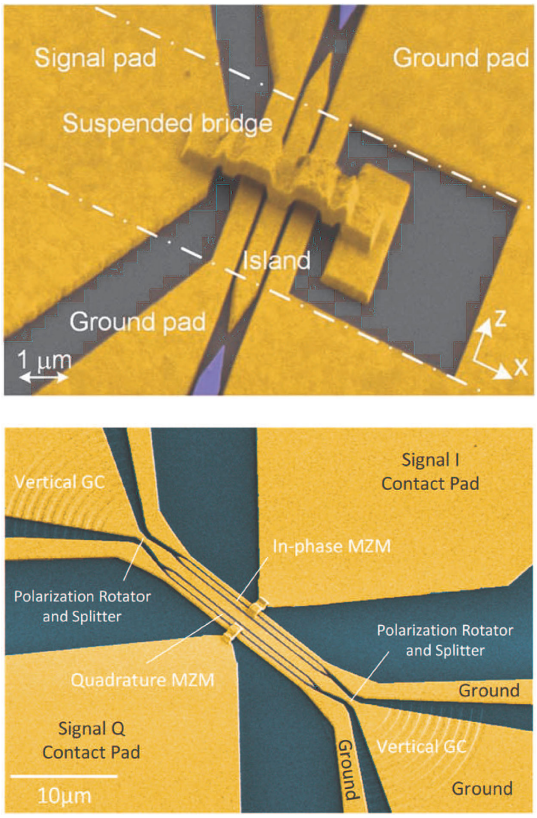

Figure 2. Examples of implementation of POH MZM. Above: colorized scanning electron microscope (SEM) image of a compact modulator with splitter/combiner integrated with the plasmonic–photonic transition (Reprinted with permission.[40] Figure 8a)Copyright 2016, IEEE). Below: Colorized SEM image of an IQ POH modulator with fiber input and output. Reproduced with permission.[41] Copyright 2019, IEEE.

the modulator had the potential of THz operation, provided that the RF electrodes were properly optimized.

In various studies,[55,56] a more relaxed layout was described somewhat similar to the one in the study by Melikyan et al.[51] with multimode interference (MMI) input and output splitters–combiners. Data modulation was demonstrated experimentally up to 72 Gbit s^{-1} (BPSK) and 108 Gbit s^{-1} (quaternary amplitude shift keying, 4-ASK) with driving voltages of $V_\pi = 4$ and 2.5 V peak to peak for modulator lengths of 12.5 and 25 μm, respectively, and slot width of 80 nm with a static extinction ratio of 25 dB (25 μm-long device) and a bandwidth in excess of 70[55] or 170 GHz.[56] The design in the study by Haffner et al.[40] reduced the slot width down to 40 nm; with 6 μm length, the record $V_\pi L$ product of 40 V μm was achieved, with an on–off voltage of 7 V and an extinction ratio in excess of 25 dB.

During the past few years, optimization of the earlier designs was further fostered by improvements in EO materials, see, for example, the study by Baeuerle et al.,[57] where a design similar to the one in the study by Heni et al.[55] is presented but optimized with a 50 nm gap and a 15 μm length to achieve 100 Gbps non-return-to-zero (NRZ) operation with an on–off voltage less than 1 V peak to peak; this allows the modulator to be directly driven by a high-speed digital circuit rather than a low-efficiency driver amplifier. The modulator fiber-to-fiber insertion loss was estimated as 11–15 dB. Further progress in the reduction of the driving voltage level was reported in other studies,[58,59] demonstrating that a peak-to-peak drive voltage of 330 m V_{pp} is sufficient to operate the plasmonic transmitter in C band at 120 Gbps non return to zero (NRZ) On-Off Keying (NRZ-OOK). A further research line concerned the development of integrated IQ modulators based on single MZ designs, see the study by Heni et al.,[60] where an IQ version of the MZMs described in the study by Heni et al.[55] was proposed, and the study by Ayata et al.[41] presenting the IQ version of the MZM in the study by Ayata et al.[61], see Figure 2, below. The modulator interaction length was 16 μm; the fiber-to-fiber losses across several devices were between 28 and 37 dB with a peak amplitude of the driving voltage, see the study by Ayata et al.[41], Section IV, $V_p = 2.5$ V. We finally mention a recent, simpler modulator concept proposed in the study by Messner et al.[62] that is based on a metal–insulator–metal (MIM) microstrip-like PS, where the OEO material is 120 nm thick and the strip width is 4 μm. The fiber-to-fiber insertion loss is 11 dB for a 11 μm shifter and modulation up to 100 Gbps is demonstrated both in the C and O band, with a peak voltage of 2.6 V.

In conclusion, POH MZMs typically exhibit outstanding $V_\pi L$ values, around 40 V μm (against the 410 V μm of the SOH modulator in the study by Kieninger et al.[32]); the intrinsic bandwidths in the THz range are also unparalleled. However, the optical insertion losses are large, so the $\alpha V_\pi L$ product is around 40 V dB (against 1 V dB for the SOH modulator in the study by Kieninger et al.[32]).

4. Modeling and Simulation of Organic MZMs

MZMs include as functional blocks an input optical splitter, an output optical combiner, and two PSs where the EO interaction takes place. Two different designs can be exploited for the PS, "concentrated" or "distributed". In the concentrated (lumped) approach the RF field phase is uniform in the EO interaction region, whereas in the distributed (TW) design the RF signal propagates along a RF quasi-transverse electromagnetic (quasi-TEM) transmission line parallel to the optical waveguide. In the lumped case, the modulator bandwidth is mainly *RC* limited by the total (generator and modulator) series resistance and modulator capacitance, whereas in the TW design limitations are due to velocity mismatch between the RF and the optical signal and RF losses, see for example, the study by Ghione[1], Section 6.5.2; additional bandwidth limitations may originate from low-pass *RC* effects in the RF transmission line. The TW design is generally expected to improve the *LB* product of the MZM (*B* modulator bandwidth), thus allowing for a decrease in V_π without compromising the bandwidth; increasing *L* is however acceptable only if the specific technology allows for a suitably low $\alpha_o L$ value.

We discuss first the case of the "concentrated" modulator. Considering that the EO organic material exhibits the Pockels EO effect, we model the variation of the local permittivity tensor $\Delta\varepsilon(\underline{r})$ as a linear function of the local and instantaneous applied field, in turn linearly depending as $\Delta\varepsilon(\underline{r}) = k v_{in}$ on the instantaneous input voltage $v_{in}(t)$ to the modulator "active region," defined as the high-RF field portion of the device where the refractive index modulation is effective. In POH and discrete, $LiNbO_3$-like MZMs, v_{in} coincides with the voltage applied to the external input of the modulator, whereas in SOH MZM, this happens only in DC, due to the *RC* partitioning between the active slot capacitance and internal parasitic resistance associated with the Si access regions to the Si modulating ribs.

The complex propagation constant of the PS optical waveguide $\gamma_o = \alpha_o + j\beta_o$ (to simplify the notation, we suppose that the two PS waveguides are not coupled) will in turn depend on $\Delta\varepsilon(\underline{r})$ and therefore on the instantaneous input voltage, that is, $\gamma_o(v_{in}(t))$. Due to the huge difference between the optical and RF frequencies, we can assume that the optical signal phase and amplitude instantaneously respond to the (slowly varying) input voltage. However, we notice that the $\gamma_o(v_{in}(t))$ dependence is, in general, not necessarily linear, even if the EO effect is linear, unless the modulator operates in small-signal conditions, that is, $v_{in}(t) = V_{in} + \hat{v}_{in}(t)$, the latter term being a small perturbation of the DC bias V_{in}. Due to the perturbatively small $\Delta\varepsilon(\underline{r})$, however, the variation of γ_o can be often approximated linearly, unless the dispersion characteristics of the optical waveguide are significantly affected by modal coupling. To better explain this remark, consider two coupled plasmonic slots with equal height and width; for $V_{in} = 0$, the structure is strictly symmetrical (due to the uniform material refractive index) and some splitting exists between the modal refractive indices of the even and odd modes. With applied push–pull voltage, the material index profile becomes asymmetrical, with increasingly localized modes, whose effective index ultimately follows the almost linear dependence in Equation (13), see Figure 10. Due to behavior of $n_{eff}(V_{in})$ around the on state $V_{in} = 0$, the linear approximation turns out to be inaccurate when simulating $T(V_{in})$ from $V_{in} = 0$ to $V_{in} = V_\pi$. Notice that the nonlinearity in $n_{eff}(V_{in})$ disappears if the plasmonic slots are uncoupled, as shown in Figure 10.

Due to the input voltage dependence of the optical complex propagation constant, the amplitude and phase of the optical field phasor at the PM output will be an instantaneous function of the input voltage as

$$\underline{E}_{o}(v_{in}(t)) = \underline{E}_{in} e^{-\alpha_o(v_{in}(t))L + j\beta_o(v_{in}(t))L} \tag{12}$$

where $\underline{E}_{in}$ is the PM input field. If we neglect the v_{in} dependence of the optical attenuation, and approximate $\beta_o(v_{in}(t))$ as a linear function of v_{in}, the output phase shift $\Delta\phi = \beta_o(v_{in}(t))L$ will be in turn a linear function of $v_{in}(t)$. The output field of the combiner is now a linear combination of the two optical fields at the combiner input ports

$$\underline{E}_{oc}(t) = S_{13}\underline{E}_{o1}(v_{in1}(t)) + S_{23}\underline{E}_{o2}(v_{in2}(t)) \tag{13}$$

where the input ports are denoted as 1 and 2, the output port is 3, and S_{ij} are the elements of the combiner S-matrix. However, the optical output power $P_{out}(t)$ depends on $|\underline{E}_{oc}(t)|^2$, thus introducing an additional nonlinear field-power block in the system. In conclusion, a concentrated modulator generally having a dual-drive configuration (with two independent input voltages) can be modeled by the block scheme shown in **Figure 3**, leading to an instantaneous, nonlinear transfer function T such as

$$p_{out}(t) = T(v_{in1}(t), v_{in2}(t))p_{in}(t) \tag{14}$$

The relationship between the two generator voltages $e_{g,i}(t)$, $i = 1, 2$ and the input voltages will be instead linear but with memory; assuming a simple RC first-order low-pass behavior we have

$$\begin{aligned} v_{in,i}(t) &= \mathcal{F}^{-1}(H_i(\omega)\mathcal{F}(e_{g,i}(t))) \\ &= \mathcal{F}^{-1}\left(\frac{\mathcal{F}(e_{g,i}(t))}{1 + j\omega R_{g,i}C_{in,i}}\right) \end{aligned} \tag{15}$$

where $\mathcal{F}$ denotes the Fourier transform, $R_{g,i}$ is the equivalent resistance of generator i, and $C_{in,i}$ is the input capacitance of PS i, assuming that the transfer function $H_i(\omega)$ can be approximated as a single-pole response. (Notice that in SOH and POH modulators no junction effects are present, thus leading to a constant capacitance model.) From a system standpoint, the lumped modulator therefore is the cascade of a linear dispersive block, see Equation (15), of a memoryless, weakly nonlinear block (describing the relationship between v_{in} and the output phase shift $\Delta\phi$), and of a memoryless, strongly nonlinear block (the field-power quadratic relationship). As Equation (6) is nonlinear but memoryless, it can be derived from a DC simulation, that is

$$T(v_{in1}(t), v_{in2}(t)) \equiv T(V_{in1}, V_{in2}) \tag{16}$$

As an example, let us consider a push–pull modulator with optically uncoupled PSs and a symmetric splitter/divider; if we neglect the splitter and combiner loss, assume that the optical attenuation is approximately voltage independent, and that β_o (and therefore $\Delta\phi$) linearly depends on v_{in}, we have

$$\begin{aligned} \frac{p_{out}(t)}{p_{in}(t)} &= \frac{1}{2}\exp(-2\alpha_o L) \\ &\times \left\{1 + \cos\left[\frac{\pi}{V_\pi}\mathcal{F}^{-1}(H(\omega)\mathcal{F}(e_g(t)))\right]\right\} \end{aligned} \tag{17}$$

where V_π is the applied voltage corresponding to π phase shift between the two shifters (i.e., $\pi/2$ for each PS), which can be estimated from electrical DC simulations, and $H(\omega)$ is a single-pole transfer function with time constant $R_g C_{in}$.

Let us now discuss the simulation strategies that may be applied to concentrated MZMs. A first approach (that we shall denote as AiO) simply consists of modeling the whole structure (splitters, PSs, combiners) as a 3D optical system, where the excitation is a mode of the input photonic waveguide and the output is a mode of the output photonic waveguide. The DC simulation requires a repeated 3D optical simulation in the presence of a local variation $\Delta\varepsilon(\underline{r})$ of the optical permittivity that can be evaluated through a "single" 3D electrical simulation. Additional complexities on the PS optical simulation posed by SOH and POH modulators are related to the nonhomogeneous anisotropy of the EO polymer as it is generated by the poling procedure. This can be in principle solved by taking into account that, as the electrical problem is almost linear, the same field pattern derived from it allows to establish the material anisotropy where the local r_{33} is directed along the static electric field lines. The dynamic (small- or large-signal) response can be finally derived by combining a nonlinear, memoryless model, see Equation (6), with the linear, dispersive model in Equation (15); the transfer function $H_i(\omega)$ between the generator voltages and the modulating voltages $v_{in,i}$ can be evaluated through a 3D frequency- or time-domain simulation. The voltage $V_{in,i}(\omega)$ can be obtained from 3D simulations as a suitable average of the electric field integral over the active region of the PS. Notice that, as the model described by Equation (14) is memoryless, the normalized small-signal frequency response is dominated by the linear-dispersive part expressed in Equation (15), that is, by $H_i(\omega)$.

An alternative line of attack to the simulation of concentrated MZMs can suitably make use of a partitioning strategy that we shall denote as DaC. In fact, independent of the technology exploited (Y junction, MMI, integration with the photonic–plasmonic transition), the splitter and combiner (the latter often being the splitter reversed) are all-optical components, which can be simulated through finite-difference time-domain (FDTD) techniques as standalone elements and characterized by their S-matrix; note that coupling between the splitter/combiner and the PS waveguides may not be limited to their fundamental mode, thus requiring the evaluation of a multimode S-matrix of the splitter/combiner, see Section 5.2. Similarly, the optical simulation of the PSs (whose structure is typically longitudinally invariant) as a standalone element may be conveniently conducted in 2D (i.e., in the cross section) rather than in 3D. To this aim, a DC 2D electrical simulation with a normalized input voltage is conducted, yielding the optical $\Delta\varepsilon(\underline{r})$ in the PS cross section; then, $\Delta\varepsilon(\underline{r})$ is scaled according to the input DC voltage(s) and an optical modal analysis is conducted, yielding γ_o for all optical propagating modes; this readily allows for the evaluation of the PS S-matrix. Also in the PS case, as PSs may be optically coupled (as often in POH modulators), their modeling implies deriving a multimode S-matrix, see Section 5.2. Cascading the PS, splitter, and combiner models finally yields the DC transfer function $T(V_{in1}, V_{in2})$, from which a small-signal or large-signal simulation can be in principle conducted according to Equations (14) and (15); the transfer function $H_i(\omega)$ can be here conveniently estimated through 2D frequency-domain electrical simulations in the PS electrical cross section.

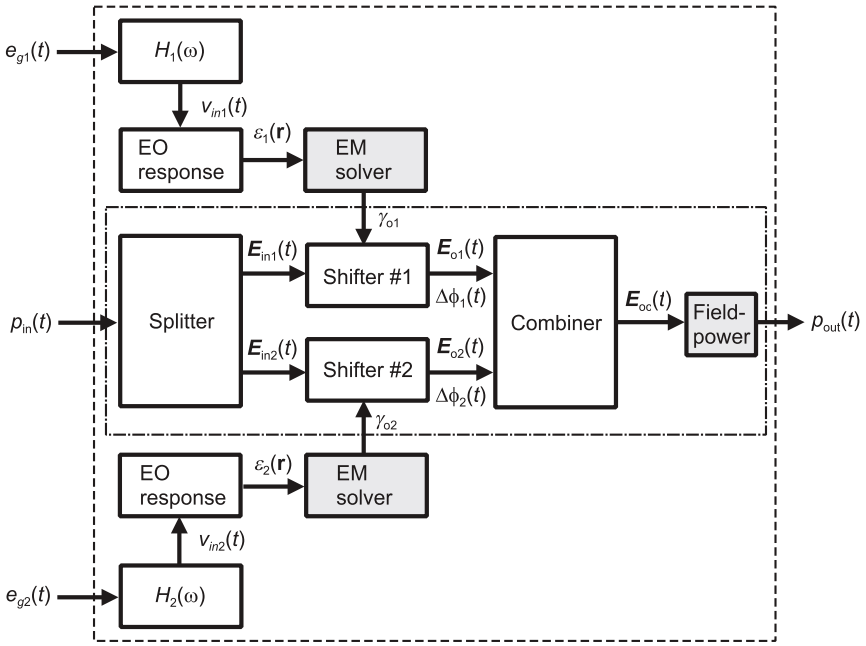

Figure 3. Block scheme of the concentrated MZ modulator model; the white boxes are linear blocks and the gray boxes are nonlinear. The dashed–dotted line encloses the part of the modulator amenable to optical simulation through an AiO approach.

Comparing the two approaches, it should be noticed that the computational intensity of the AiO approach can be quite prohibitive already for modulator lengths of the order of 10 μm, that are typical in POH modulators, let alone for SOH devices where the interaction length is at least ten times longer ($L \approx n\lambda_o$ with $n > 100$ typically, λ_o optical wavelength). Consider also that in the AiO approach the excitation of the output fundamental mode in the output photonic waveguide may require additional care, as, due to the size limitations of the computational domain, the simulation may not accurately reproduce the fact that at the output of the combiner, part of the optical field is radiated rather than coupled to the fundamental mode of the output photonic waveguide. In practice, POH is the only MZM class to which the AiO approach can be applied.

With respect to the concentrated case, the simulation of TW (distributed) modulators poses additional problems. As at DC no distributed effects arise, deriving the static transfer function $T(V_{in1}, V_{in2}) \equiv T(E_{g1}, E_{g2})$ can be done exactly as in the lumped case. However, the AiO approach fails to provide a viable solution to the dynamic modeling of such modulators, where a continuous, TW interaction occurs between the RF and optical signals, as schematically shown in **Figure 4**. This would require simulating, for example through FDTD, the simultaneous propagation of two interacting signals (optical and RF) having widely different frequency ranges, thus requiring integration times related to a fraction of the optical wave period but total simulation times of a few periods of the RF wave, which is practically unfeasible in 3D. Thus, the only practical solution to the dynamic simulation of TW modulators is to exploit a DaC approach, modeling the

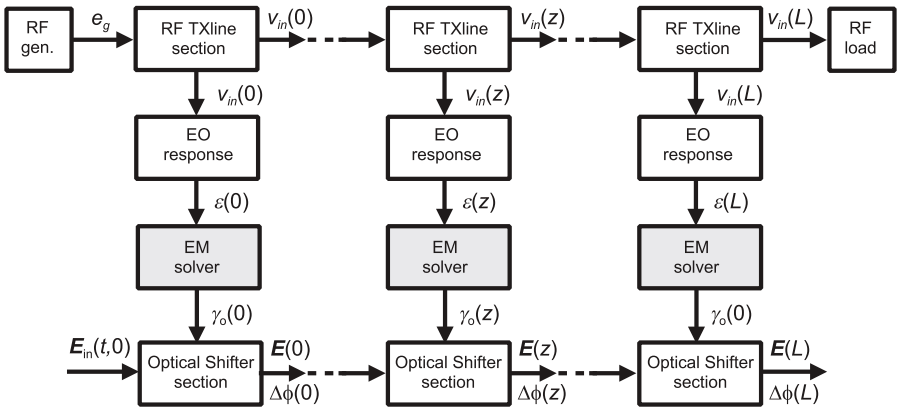

Figure 4. Block scheme of the PS block of a distributed organic MZ modulator model; the white boxes are linear blocks and the gray boxes are nonlinear. Notice that in many modulator implementations involving junctions (III–V or Si), the RF transmission line becomes nonlinear.

PSs as coupled electrical and optical waveguides in 2D. Concerning the TW PS dynamic simulation, some cases are amenable to a partly closed-form solution. If the dependence of γ_o on the local electric field is approximated as linear (this is always true in small-signal conditions), the PS can be modeled as a linear system with memory following the approach, for example, in the study by Ghione,[1] Section 6.5. For a symmetric push–pull MZM with uncoupled optical PS waveguides, the frequency-dependent complex modulation index $m(\omega)$ reads

$$m(\omega) = K(\omega)\frac{R_L + R_g}{R_L}\frac{Z_{in}}{Z_{in} + Z_g} \times \frac{(Z_L + Z_0)F(u_+) + (Z_L - Z_0)F(u_-)}{(Z_L + Z_0)e^{\gamma_{RF}L} + (Z_L - Z_0)e^{-\gamma_{RF}L}} \tag{18}$$

where $K(\omega)$ is a low-pass filter with $V_{in} = K(\omega)V_{RF}$, where V_{RF} is the RF line voltage, R_L (Z_L) and R_g (Z_g) are the generator and load resistances (impedances), and γ_{RF} is the complex propagation constant of the RF line

$$\gamma_{RF} = \alpha_{RF} + j\beta_{RF} = \alpha_{RF} + j\omega/v_{RF} \tag{19}$$

L is the EO interaction length, and

$$F(u) = \frac{1 - \exp(u)}{u} \tag{20}$$

$$u_\pm(\omega) = j(\pm\beta_{RF} - \beta_o)L \pm \alpha_{RF}L \tag{21}$$

$$Z_{in} = Z_0\frac{Z_L + Z_0\tanh(\gamma_{RF}L)}{Z_0 + Z_L\tanh(\gamma_{RF}L)} \tag{22}$$

where Z_{in} is the input impedance of the PS RF line and Z_0 is the PS RF characteristic impedance. As the combiner is a nonlinear, memoryless element, the small-signal modulator frequency response will only depend on the PS response, see Equation (18).

In the earlier conditions, that is, if the dependence of γ_o on $\Delta\varepsilon$ (and therefore on the local phasors $V_{in}(z)$ and $V_{RF}(z)$ and generator voltage E_g) can be approximated as linear, the general dynamic response of the TW MZM can be obtained considering that the phase shift can be expressed as

$$\Delta\phi(\omega) = \frac{\pi n_o^3 r_{33}}{\lambda_o}\Gamma_{RF|o}\frac{L}{G}m(\omega)E_g \equiv H(\omega)E_g \tag{23}$$

where n_o is the optical refractive index, G the gap between the modulator electrodes, and $\Gamma_{RF|o}$ the overlap integral between the optical and RF fields (Equation (23) strictly applies when the variation of the optical effective index equals the variation of the material index, as in weakly guiding $LiNbO_3$ optical waveguides; in general, a proportionality factor should be added, that can be included formally into the overlap integral). Under these conditions, the general dynamic response can be expressed as in Equation (17).

The models described by Equations (18) and (23) can be in principle extended to the case where PSs are coupled and Equation (17) is replaced by a more complex S-matrix model for the combiner, the only constraint being the linear and instantaneous dependence of γ_o on V_{in}. If this condition is not met (as it happens in structures where the EO effect is not linear, like InP or Si junction-based MZMs) and/or if the PS line is nonlinear due to the presence of a junction capacitance, the dynamic simulation of TW MZMs requires a discrete pseudolumped cascaded cell model of the PS.

From the earlier discussion, we can conclude that the AiO approach is hardly applicable to the simulation of TW MZMs (computationally heavy for the DC transfer curve, inapplicable for dynamic modeling), the DaC being therefore the suggested modeling strategy. An example of the DaC modulator model including two linear-distributed PSs and implemented within the Microwave Office circuit environment was presented in the study by Pirola et al.,[63] whereas the discrete cell approach to nonlinear and/or strongly RF-dispersive PS simulation is similar to the one presented in the study by Cappelluti et al.[64] for the dynamic modeling of InP-based EAMs.

The models in various studies[63,64] are also examples of system-level models whose parameters can be derived by physics-based approaches applied to part of the structure. This approach is also commonly implemented in well-known commercial simulators like Lumerical[65] or Synopsis RSoft CAD.[66] A different system-level approach, outlined in the study by Ghione et al.,[67] bases the time-domain dynamic simulation on an entirely black-box model, corresponding to the dashed line in Figure 3, where

$$p_{out}(t) = T\left(v_{in1}(t), v_{in2}(t), p_{in}(t), \frac{d}{dt}\right) \tag{24}$$

which has to be fitted or trained on physics-based simulation or measurements. The preliminary results presented in the study by Ghione et al.[67] and summarized in Section 5.3 show that neural networks provide an accurate and efficient behavioral modulator model, at least for the lumped case.

5. Examples

In this section we will present examples of physics-based modeling of SOH (Section 5.1) and POH (Section 5.2) EO MZMs, with an aim at stressing the peculiarities found and challenges met in simulating typical examples of the two modulator classes. Section 5.3 is devoted to preliminary results on neural network, system-level behavioral modeling of MZMs, a general strategy that can be applied to the simulation of modulators independent of the technological details.

5.1. Silicon Organic Hybrid MZM's Physics-Based Modeling

As a case study, we will focus on a device similar to the one presented in various studies[36,68] operating at 1.55 μm. The structure is defined on a SiO_2 layer. Each arm of the MZM is realized with a 100 nm-wide slot waveguide defined by two heavily doped ($N_D = 7 \times 10^{17}\,cm^{-3}$) Si rails having 210 nm height and width. The device is covered by a layer of DLD-164 NLO polymer. The RF field inducing the EO effect is brought to the rails through Si films with 60 nm thickness and the same doping of the rails, biased by Au contacts. It is to be noted that this choice of the geometrical parameters, quite different from those of the ones in the study by Palmer et al.[68] (in particular for the slot width), facilitates a comparison with the POH

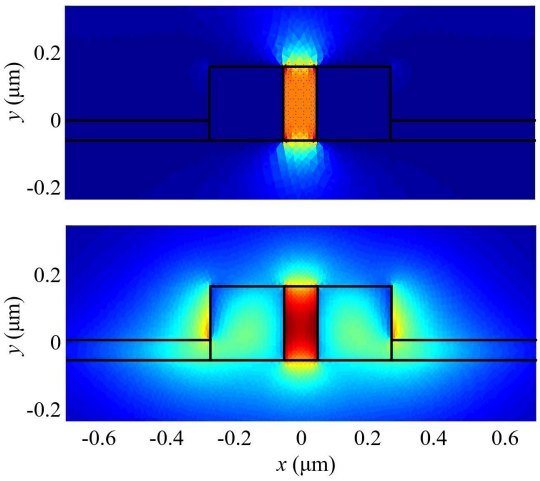

Figure 5. Color maps of the x component of the electric field. Above: Low-frequency RF field. Below: Optical field at $\lambda = 1.55$ μm.

modulator example presented in Section 5.2. Optical power splitters/recombiners are realized by MMI couplers that are considered here as ideal.

Because of its very large footprint, the device under study can be simulated only by means of a DaC approach. The following strategy has been adopted. First, an electric simulation is conducted to determine the RF field. As Si doping is uniform, the semiconductor is modeled as a conductor, with effective conductivity $\sigma = q\mu_n N_D$, where q is the elementary charge, N_D is the Si donor doping, and μ_n is the Si electron mobility, assumed as 1200 $cm^2\,(Vs)^{-1}$. This allows to reduce the electrical analysis to a quasistatic problem in the 2D cross section. The simulated RF field distribution is shown in **Figure 5** (above). The simulation has been conducted in quasistatic conditions; however, the RF field profile in the slot does not appreciably vary with frequency, although it decreases above the cutoff due to the effect of the large slot capacitance. The frequency response is in fact dominated by the *RC* effect of the slot capacitance and the parallel resistance of the Si rails. In the second step, the quasistatic electric field is used to evaluate the change of refractive index inside the slot, $\Delta n_{mat}(x, y)$, according to Equation (5), for $r_{33} = 180$ pm V^{-1}, leading to

$$n_{mat,EO} = n_{mat} + \Delta n_{mat} \approx 1.83 + 5.5156 \times 10^{-3} V_{in} \tag{25}$$

where V_{in} is the slot voltage. Then, for each RF voltage V_{RF} applied to the contacts, the corresponding Δn_{mat} is used as input of an electromagnetic (EM) mode solver. At optical frequencies, $n_{Si} = 3.47$, and the losses introduced by doping have been estimated to be 5 cm^{-1} from the study by Soref et al.[69] The outputs of the EM solver are the optical effective refractive index $n_{eff}(V_{RF})$ and the losses $\alpha(V_{RF})$ for the fundamental slot mode, whose topography is shown at $V_{RF} = 0$ V in Figure 5 (below). Even if guiding is dominated by the Si (highest) refractive index, the field is found to be maximum between the rails. This can be interpreted as a consequence of the continuity of the electric displacement vector component $\mathcal{D}_x = \varepsilon \mathcal{E}_x$, and of the proximity of the two rails. Nevertheless, it can be noted that the optical field is quite strong also in the rails. In this view, only part of the electric field overlaps with the RF field, which instead is well confined within the slots, limiting the effectiveness of the EO optical index modulation.

Because the MZM slots are distant several tens of μm, no coupling between the optical waveguides in the PSs can take place. As coupling is negligible, the optical field topography does not exhibit significant deviations with respect the 0 V case when applying a bias. Moreover, the EM simulations reveal that n_{eff} depends linearly on V_{RF}, leading, for the device under study, to the fitting expressions

$$n_{eff,1|2} = 2.2610 \mp 1.1155 \times 10^{-3} V_{RF} \tag{26}$$

where the subscripts 1 (2) refer to the left (right) slot, respectively. The effective refractive index without applied bias is found to be higher than that of the EO material, which confirms the interpretation according to which guiding is enabled by the Si rails. This result allows to evaluate immediately V_π; recalling that

$$\Delta\phi = k_0 L \left| n_{eff,1}(V_{RF}) - n_{eff,2}(V_{RF}) \right| \tag{27}$$

and solving for $\Delta\phi = \pi$, we obtain $V_\pi L = 0.35$ V mm. The small deviation of this estimate from the experimental values[68] can be ascribed to the different geometrical parameters.

From the mode effective refractive index and losses, it is also possible to compute, with Equation (17) evaluated at $\omega = 0$, the static modulator response, which is shown in **Figure 6**, for a modulator with length $L = 1$ mm. The simulated extinction ratio is not realistic, as the combiner nonidealities have been neglected in the closed-form model of Equation (17).

As the modulator length is typically much shorter than the RF wavelength, the frequency response can be approximated according to a lumped approach. Here, the RF voltage between the gold strips undergoes a frequency-dependent partitioning that leads to a frequency-dependent slot modulating voltage V_{in}. To account for this in the concentrated modulator, the frequency-dependent per-unit-length (p.u.l.) series impedance and parallel admittance of the quasi-TEM line are evaluated from an EM solver[70,71] and shown in **Figure 7** for the device under study. Then, the parallel admittance of the lumped equivalent circuit in **Figure 8** (inset) is

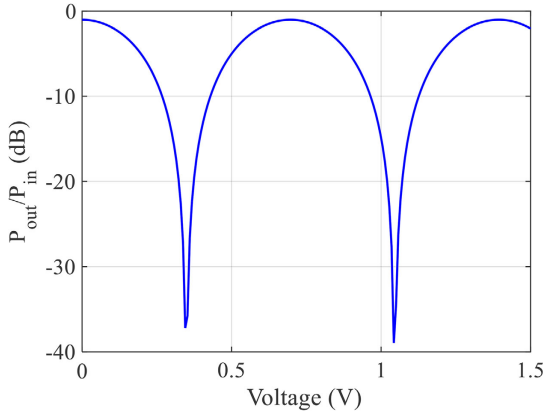

Figure 6. Static response of the SOH modulator under study, for $L = 1$ mm.

fitted by the R_1C_1 parallel branch (where C_1 indicates the slot capacitance). The red dashed lines in Figure 7 are reported to demonstrate how the lumped conductance and capacitance overlap perfectly with the results of the quasi-TEM simulation. Finally, the frequency response for a 300 μm MZM is shown in Figure 8; the (optical) 3 dB bandwidth around 30 GHz is consistent with the experimental estimates on similar geometries and is mainly related to the effect of the R_1C_1 time constant, depending both on the slot width and on the doping of the Si thin (here, $t = 60$ nm) access layer to the Si rails. Increasing t decreases the R_1C_1 time constant, thus improving the bandwidth, but at the same time decreases the optical field confinement and increases the $V_\pi L$ product; the choice of t thus implies a careful tradeoff between the MZM speed and on–off voltage.

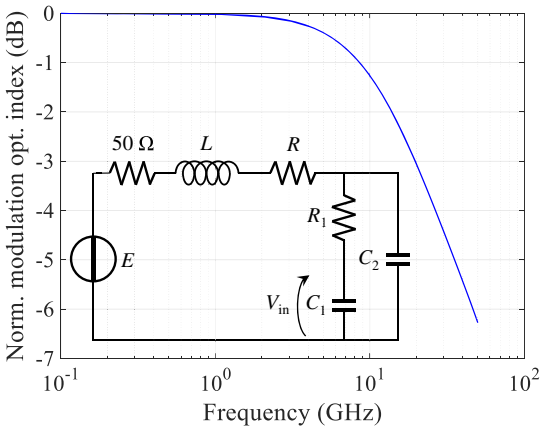

Figure 8. Frequency response of the modeled SOH MZM evaluated with the one-cell equivalent circuit shown in the inset. The assumed modulator length is 300 μm. The equivalent circuit parameters L and R are frequency dependent according to the results of the quasistatic model (see Figure 7). $R_1 = 200\,\Omega$, $C_1 = 62$ fF, and $C_2 = 12.4$ fF.

5.2. Plasmonic Organic Hybrid MZM's Physics-Based Modeling

This section presents a comparison of AiO and DaC simulation strategies, applied to a POH EO MZM similar to the one presented in various studies.[53,72] The structure is defined on a 3 μm-thick SiO_2 layer lying on a Si substrate. The two arms of the MZM are slot waveguides, defined by the central gold island (500 nm thick) and the two lateral gold rails (each one 520 nm thick). In this case study, all the gold layers are 220 nm high, and the slots are 100 nm wide. The optical input signal is assumed to be the fundamental mode of the input (left) Si waveguide. This mode reaches a splitter, consisting of two facing tapers (left in Si and right in Au) and converting the dielectric waveguide mode into the slot plasmonic modes. The structure is symmetric with respect to the central z-section (the center of the gold island) so that, after propagating in the slots, the plasmonic modes are recombined and coupled to the output Si waveguide. The device is covered by a layer of DLD-164 NLO polymer, with thickness $h_{NLO} = 300$ nm measured from the SiO_2 end. The phase modulators are driven in push–pull operation by a single signal, using the coplanar ground–signal–ground transmission

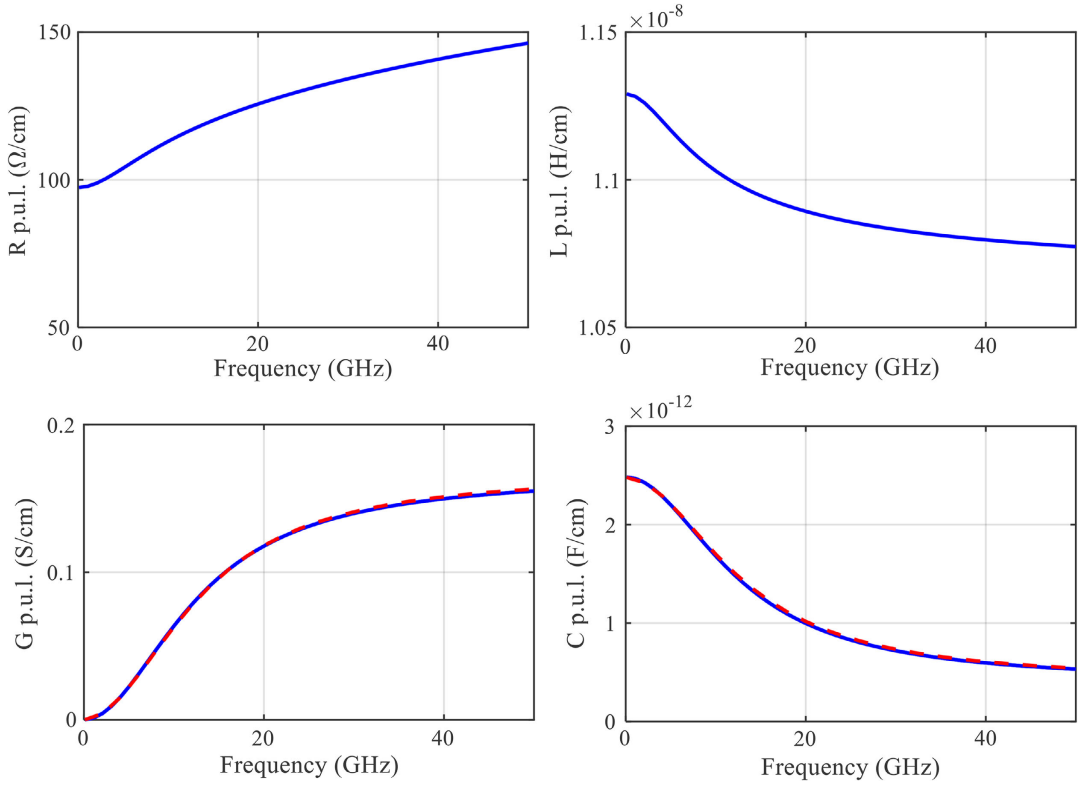

Figure 7. Per-unit-length parameters of the SOH electrodes from EM simulation (continuous line). Per-unit-length conductance and capacitance fitted from the equivalent circuit in Figure 8, see inset (dashed line).

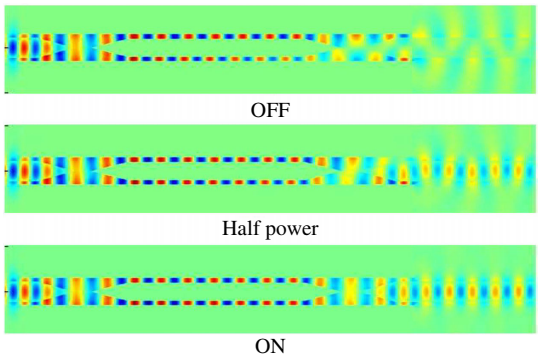

Figure 9. Color maps of the real part of the transverse electric field $\mathcal{E}_x$ from full 3D FDTD simulations.[65] Above: off state; middle: half-power state; below: on state.

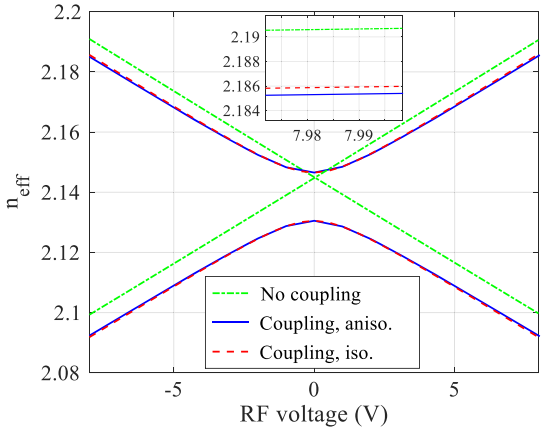

Figure 10. Optical effective refractive index versus RF voltage. The green dashed curves are obtained by simulating two isolated slots. The solid blue and red dashed curves have been obtained from simulations of the entire cross section of the POH MZM phase modulator, considering the EO material as anisotropic or approximating it as isotropic. The inset shows a magnification around $V_{RF} = 8$ V, to emphasize the slight difference between the isotropic/anisotropic cases.

line shown in Figure 1 (above).[12,73–75] This is obtained by aligning the poling field for the EO polymer to the modulation RF field, the latter having opposite polarity in each modulator arm.

Figure 9, which shows the real part of $\mathcal{E}_x$, demonstrates how modulation can be achieved through the EO effect induced by the RF voltage applied to the central island contact. In the off state (top panel), the fields in the two branches clearly have opposite phases, leading to destructive interference and radiation out of the output waveguide. If the fields are in phase at the output coupling section (bottom panel), the MZM output is maximum and it operates in the on state. The middle panel shows an intermediate condition, that is, the half-power operation. If the slot dimensions are equal, the on state is at $V_{RF} = 0$ V. However, the MZM can be also designed to operate around the quadrature point (where linearity is maximum) at zero bias voltage,[53,72] by choosing different slot widths.

In addition to the AiO approach behind the results of Figure 9, the device under study has been analyzed also with a DaC strategy. To this aim, the first step requires evaluating the optical waveguide parameters for different RF electric field intensities. In this view, **Figure 10** shows the effective refractive index $n_{\text{eff}}(V_{RF})$. Three groups of curves are presented, to provide a discussion of the underlying approximations. In particular, the dash–dotted green curves have been obtained neglecting optical coupling between the slots, that is, by conducting two different simulations, each one including just one slot. The solid blue and dashed red curves, both including slot coupling effects, are obtained with and without including the position-dependent anisotropy of the EO polymer. It is apparent that treating the material as isotropic leads only to a slight overestimation of the electro/optic effect. In contrast, the anticrossing-like behavior of n_{eff} in the proximity of the on state ($V_{RF} = 0$ V in this example) is very different from the linear response of the uncoupled case: mode coupling plays a major role, resulting, as already remarked, in a global nonlinear dependence of the optical waveguide parameters on the RF driving voltage.

For large V_{RF}, the curves are asymptotically linear, with the same slope. In this view, the straight lines allow a fair comparison of the EO effect with the SOH case. Here, we have

$$n_{\text{eff},1|2} = 2.144 \mp 5.7032 \times 10^{-3} V_{RF}. \tag{28}$$

The linear coefficient in Equation (28) is about 6 times the corresponding one in Equation (26), relative to the SOH MZM, consistent with the fact that in the POH MZM, the overlap between the RF and optical fields is much better than that in the POH MZM.

Because of mode coupling, the MZM response cannot be obtained by exploiting the simple combiner model in Equation (17). This model does not account for the bias dependence of the PS modes, whose topography, as already remarked, is even/odd at the on state (where strong mode coupling occurs due to the symmetry in the refractive index distribution) but becomes increasingly localized away from the on state (where coupling is weaker due to the asymmetrical refractive index distribution induced by the EO effect). To model these effects adequately, a bimodal picture of the MZM is required,[76] where the transmission lines describing the propagation of the optical

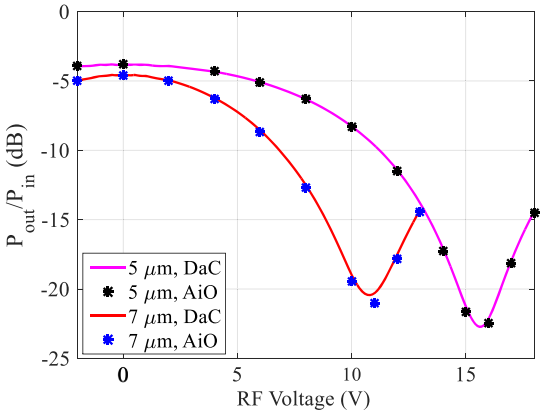

Figure 11. $P_{\text{out}}/P_{\text{in}}$ characteristics obtained with the AiO full 3D FDTD simulations (markers) and with the DaC approach (solid lines) presented in this work for two modulators with $L = 5$ and 7 μm.

modes are coupled by the 3×3 scattering matrices characterizing the splitter/recombiner.[72] This approach has been used to generate the results in **Figure 11**, which shows a comparison of AiO and DaC simulations. From this figure, we deduce the value $V_\pi L \simeq 80$ V mm, much lower than that of the SOH result. In contrast, optical losses are much worse than in the SOH case already for $V_{RF} = 0$ V. Mode coupling also negatively affects the extinction ratio.

It is to be remarked that each V_{RF} point in the AiO approach requires a 3D FDTD simulation of the entire device, so evaluating the MZM response in the few points shown in the figure requires several days. In contrast, the DaC approach[72] requires a single 3D FDTD of the splitter section only and few 2D mode computations, which can be interpolated to achieve the final response for a very large number of RF voltages at almost no computational cost.

5.3. MZM Behavioral Modeling

System-level simulations of the entire chain (Tx/fiber/Rx) of an optical telecommunication system require computationally-efficient models to allow for simulating the link response to huge input data streams, possibly modulated with multilevel formats. To this aim, rather than inserting directly physics-based models in the simulation flow, a possible alternative could be to use behavioral models. In this section, we present an example of behavioral modeling solution for a MZM modulator with a concentrated design. The model input is a time series of input voltages, generated at random according to a modulation format, whereas the output is the resulting instantaneous optical power.

Building a system-level model requires 1) to choose a suitable class of behavioral models, 2) to train the model, through numerical optimization, to reproduce the output characteristics of the device under study due to a known input referred to as "training sequence," and 3) to validate the trained model by verifying that it can reproduce the input/output characteristics for a "validation sequence," different from the training sequence.

From the discussion in Section 4, it is clear that both MZMs based on OEO materials and on EO dielectrics like $LiNbO_3$ can be modeled, in general dynamic conditions, as two cascaded blocks: the first, linear and with memory (the PS) and the second, memoryless but nonlinear (the output combiner). In this view, nonlinear autoregressive exogenous neural networks (NARXnets) appear to be a convenient platform.[77]

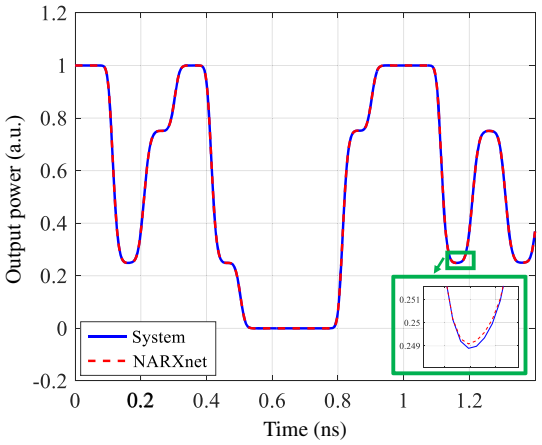

Figure 13. Comparison between the modulator model output power (in arbitrary units) due to the validation sequence (solid blue curve) and the corresponding results achieved from the neural network behavioral model (dashed red curve). The inset presents a magnification in the neighborhood of a transition, to provide a visual representation of the deviation between the two curves, which can be quantified, in norm 2, to be about 0.015%.

An example of application is now discussed: the considered input is a 20 Gbps 4-level pulse amplitude modulation (PAM4) pseudorandom sequence smoothed with a Gaussian filter emulating the finite bandwidth of the signal generator. The modulator training and comparison data are generated by a physics-based model of a structure similar to the one discussed in Section 5.2, that is, a damped second-order system with 20 GHz cutoff frequency for the PS and the model in Equation (17) for the combiner.

NARXnet has been implemented with the MATLAB Deep Learning Toolbox.[78] The network diagram is shown in **Figure 12**: the hidden layer includes three neurons, such that the inputs are subjected to 1−4 delays (the exact number is one of the degrees of freedom). Both open- and closed-loop trainings are conducted on a 9 ns sequence by the Levenberg–Marquardt algorithm, aiming to minimize the mean squared error. As a final result, **Figure 13** shows the comparison of the system output (solid

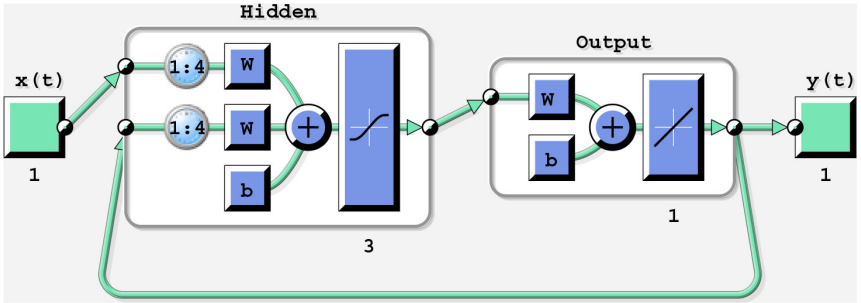

Figure 12. Schematic of the NARX neural network designed for the example in Section 5.3. The hidden layer consists of three neurons, where each of the inputs is subjected to 1−4 delays (exact number chosen as a result of the training).

blue curve) with the results of the behavioral model (dashed red curve) for a validation sequence lasting for 1.4 ns. The very good agreement of the curves, whose norm 2 deviation is about 0.015%, demonstrates the feasibility of this approach.

6. Conclusion

MZ EOMs based on organic electro-optic materials are among the most interesting solutions for the development of optical modulators compatible with a Si photonic platform. Innovative MZM designs based on plasmonic waveguides have been extensively developed within this framework. In this article, we have tried to provide a synthetic overview on the issues involved in the static and dynamic simulation of this class of modulators, from the physical to the system level. We have shown in particular that a general AiO strategy based on 3D multiphysics simulation tools has to be often replaced or assisted, for reasons mainly (but not solely in the TW MZMs case) related to computational intensity, by ad hoc DaC strategies, which have often to be tuned or adapted to individual device classes. Finally, neural network behavioral modeling, on which we have provided some preliminary results, appears promising for system-level, technology-independent modulator simulation.

Acknowledgements

The work was in part funded by HiSilicon (grant number HIRPO2017030805-Modelling of integrated Mach-Zehnder electrooptic modulators: from materials to system-level design).

Open Access Funding provided by Politecnico di Torino within the CRUI-CARE Agreement.

Conflict of Interest

The authors declare no conflict of interest.

Keywords

electro-optic modulators, Mach–Zehnder modulators, organic electro-optic materials, plasmonics, Si photonics

Received: June 23, 2021
Revised: July 30, 2021
Published online:

[1] G. Ghione, *Semiconductor Devices for High-Speed Optoelectronics*, Cambridge University Press, Cambridge, UK **2009**.
[2] A. Chen, E. Murphy, *Broadband Optical Modulators: Science, Technology, and Applications*, CRC Press, Boca Raton, FL **2011**.
[3] K. Wakita, *Semiconductor Optical Modulators*, Springer Science & Business Media, New York **2013**.
[4] L. Arizmendi, *Phys. Status Solidi A* **2004**, *201*, 253.
[5] B. Jalali, *Phys. Status Solidi A* **2008**, *205*, 213.
[6] O. Westreich, G. Atar, Y. Paltiel, N. Sicron, *Phys. Status Solidi A* **2018**, *215*, 1700551.
[7] L. Chrostowski, M. Hochberg, *Silicon Photonics Design: From Devices to Systems*, Cambridge University Press, Cambridge **2015**.
[8] L. Vivien, L. Pavesi, *Handbook of Silicon Photonics*, Taylor & Francis, Boca Raton, FL **2016**.
[9] A. Rahim, A. Hermans, B. Wohlfeil, D. Petousi, B. Kuyken, D. Van Thourhout, and R. Baets, *Adv. Photon.* **2021**, *3*, 024003.
[10] W. Barford, *Electronic and Optical Properties of Conjugated Polymers*, International Series of Monographs on Physics, vol. *159*, Oxford University Press, Oxford **2013**.
[11] I. Rau, L. Puntus, F. Kajzar, *Mol. Cryst. Liq. Cryst.* **2019**, *694*, 73.
[12] H.-W. Chen, J. D. Peters, J. E. Bowers, *Opt. Express* **2011**, *19*, 1455.
[13] M. Jazbinsek, U. Puc, A. Abina, A. Zidansek, *MDPI Appl. Sci.* **2019**, *9*, 882.
[14] I. Pinto, A. Sasso, S. Tosca, *Il Nuovo Cimento B (1971-1996)* **1982**, *70*, 31.
[15] R. W. Boyd, *Nonlinear Optics*, Academic Press, London **2020**.
[16] A. Yariv, P. Yeh, *Optical Waves in Crystals*, vol. *5*, Wiley, New York **1984**.
[17] H. Xu, D. Yang, F. Liu, M. Fu, S. Bo, X. Liu, Y. Cao, *Phys. Chem.* **2015**, *17*, 679.
[18] F. Kajzar, K.-S. Lee, A. K.-Y. Jen, in *Polymers for Photonics Applications II* (Ed.: K.-S. Lee), Springer, Berlin, Heidelberg **2003**, pp. 1–85.
[19] L. Dalton, in *Polymers for Photonics Applications I* (Ed.: K.-S. Lee), Springer, Berlin, Heidelberg **2002**, pp. 1–86.
[20] W. Heni, C. Haffner, D. L. Elder, A. F. Tillack, Y. Fedoryshyn, R. Cottier, Y. Salamin, C. Hoessbacher, U. Koch, B. Cheng, B. Robinson, L. R. Dalton, *Opt. Express* **2017**, *25*, 2627.
[21] D. G. Girton, S. L. Kwiatkowski, G. F. Lipscomb, R. S. Lytel, *Appl. Phys. Lett.* **1991**, *58*, 1730.
[22] D. Chen, H. R. Fetterman, A. Chen, W. H. Steier, L. R. Dalton, W. Wang, Y. Shi, *Appl. Phys. Lett.* **1997**, *70*, 3335.
[23] W. Wang, Y. Shi, D. J. Olson, W. Lin, J. Bechtel, *IEEE Photon. Technol. Lett.* **1999**, *11*, 51.
[24] J. Mallari, C. Wei, D. Jin, G. Yu, A. Barklund, E. Miller, P. O'Mathuna, R. Dinu, A. Motafakker-Fard, B. Jalali, in *2010 Conference on Optical Fiber Communication (OFC), collocated National Fiber Optic Engineers Conference (OFC/NFOEC)*, IEEE, Piscataway, NJ **2010**, pp. 1–3.
[25] S. R. Nuccio, R. Dinu, B. Shamee, D. Parekh, C. Chang-Hasnain, A. Willner, in *Optical Fiber Communication Conf.*, Optical Society of America, Washington, DC **2011**, p. JThA030.
[26] D. Jin, H. Chen, A. Barklund, J. Mallari, G. Yu, E. Miller, R. Dinu, in *Organic Photonic Materials and Devices XII*, vol. *7599*, International Society for Optics and Photonics, Bellingham, WA **2010**, p. 75990H.
[27] H. Miura, F. Qiu, A. M. Spring, T. Kashino, T. Kikuchi, M. Ozawa, H. Nawata, K. Odoi, S. Yokoyama, *Opt. Express* **2017**, *25*, 28.
[28] S. Michel, J. Zyss, I. Ledoux-Rak, C. T. Nguyen, in *Organic Photonic Materials and Devices XII*, vol. *7599*, International Society for Optics and Photonics, Bellingham, WA **2010**, p. 75990I.
[29] X. Zhang, B. Lee, C.-y. Lin, A. X. Wang, A. Hosseini, R. T. Chen, *IEEE Photon. J.* **2012**, *4*, 2214.
[30] E. Nitiss, A. Tokmakovs, K. Pudzs, J. Busenbergs, M. Rutkis, *Opt. Express* **2017**, *25*, 31036.
[31] H. Sato, H. Miura, F. Qiu, A. M. Spring, T. Kashino, T. Kikuchi, M. Ozawa, H. Nawata, K. Odoi, S. Yokoyama, *Opt. Express* **2017**, *25*, 768.
[32] C. Kieninger, C. Füllner, H. Zwickel, Y. Kutuvantavida, J. N. Kemal, C. Eschenbaum, D. L. Elder, L. R. Dalton, W. Freude, S. Randel, C. Koos, *Opt. Express* **2020**, *28*, 24693.

[33] J. Leuthold, W. Freude, J.-M. Brosi, R. Baets, P. Dumon, I. Biaggio, M. L. Scimeca, F. Diederich, B. Frank, C. Koos, *Proc. IEEE* **2009**, *97*, 1304.
[34] R. Ding, T. Baehr-Jones, Y. Liu, R. Bojko, J. Witzens, S. Huang, J. Luo, S. Benight, P. Sullivan, J.-M. Fedeli, M. Fournier, L. Dalton, A. Jen, M. Hochberg, in *2010 7th IEEE Int. Conf. on Group IV Photonics (GFP)*, IEEE, Piscataway, NJ **2010**, pp. 201–203.
[35] R. Himmelhuber, O. D. Herrera, R. Voorakaranam, L. Li, A. M. Jones, R. A. Norwood, J. Luo, A. K.-Y. Jen, N. Peyghambarian, *J. Lightwave Technol.* **2013**, *31*, 4067.
[36] R. Palmer, L. Alloatti, D. Korn, P. C. Schindler, M. Baier, J. Bolten, T. Wahlbrink, M. Waldow, R. Dinu, W. Freude, C. Koos, J. Leuthold, *IEEE Photon. Technol. Lett.* **2013**, *25*, 1226.
[37] L. Alloatti, R. Palmer, S. Diebold, K. P. Pahl, B. Chen, R. Dinu, M. Fournier, J.-M. Fedeli, T. Zwick, W. Freude, C. Koos, J. Leuthold, *Light Sci. Appl.* **2014**, *3*, 173.
[38] C. Kieninger, Y. Kutuvantavida, D. L. Elder, S. Wolf, H. Zwickel, M. Blaicher, J. N. Kemal, M. Lauermann, S. Randel, W. Freude, L. Dalton, C. Koos, *Optica* **2018**, *5*, 739.
[39] S. Wolf, H. Zwickel, W. Hartmann, M. Lauermann, Y. Kutuvantavida, C. Kieninger, L. Altenhain, R. Schmid, J. Luo, A. K.-Y. Jen, S. Randel, W. Freude, C. Koos, *Sci. Rep.* **2018**, *8*, 2598.
[40] C. Haffner, W. Heni, Y. Fedoryshyn, A. Josten, B. Baeuerle, C. Hoessbacher, Y. Salamin, U. Koch, N. Djordjević, P. Mousel, R. Bonjour, A. Emboras, D. Hillerkuss, P. Leuchtmann, D. L. Elder, L. R. Dalton, C. Hafner, J. Leuthold, *Proc. IEEE* **2016**, *104*, 2362.
[41] M. Ayata, Y. Fedoryshyn, W. Heni, A. Josten, B. Baeuerle, C. Haffner, C. Hoessbacher, U. Koch, Y. Salamin, D. L. Elder, L. R. Dalton, J. Leuthold, *J. Lightwave Technol.* **2019**, *37*, 1492.
[42] J. Leuthold, R. Bonjour, Y. Salamin, C. Hoessbacher, W. Heni, C. Haffner, A. Josten, B. Baeuerle, M. Ayata, A. Messner, U. Koch, T. Watanabe, Y. Fedoryshyn, P. Ma, M. Burla, D. L. Elder, L. R. Dalton, in *2018 Optical Fiber Communications Conf. and Exposition (OFC)*, IEEE, Piscataway, NJ **2018**, pp. 1–3.
[43] C. Haffner, D. Chelladurai, Y. Fedoryshyn, A. Josten, B. Baeuerle, W. Heni, T. Watanabe, T. Cui, B. Cheng, S. Saha, D. L. Elder, L. R. Dalton, A. Boltasseva, V. M. Shalaev, N. Kinsey, J. Leuthold, *Nature* **2018**, *556*, 483.
[44] W. Cai, J. S. White, M. L. Brongersma, *Nano Lett.* **2009**, *9*, 4403.
[45] X. Sun, L. Zhou, H. Zhu, Q. Wu, X. Li, J. Chen, *IEEE Photon. J.* **2014**, *6*, 1.
[46] J. Choe, J. T. Kim, *IEEE Photon. Technol. Lett.* **2015**, *27*, 514.
[47] J. T. Kim, *IEEE J. Select. Topics Quantum Electron.* **2015**, *21*, 184.
[48] M. Sun, W. Shieh, R. R. Unnithan, *IEEE Photon. J.* **2017**, *9*, 1.
[49] H. Dalir, F. Mokhtari-Koushyar, I. Zand, E. Heidari, X. Xu, Z. Pan, S. Sun, R. Amin, V. J. Sorger, R. T. Chen, *Nanophotonics* **2018**, *7*, 859.
[50] A. Messner, F. Eltes, P. Ma, S. Abel, B. Baeuerle, A. Josten, W. Heni, D. Caimi, J. Fompeyrine, J. Leuthold, *J. Lightwave Technol.* **2019**, *37*, 281.
[51] A. Melikyan, L. Alloatti, A. Muslija, D. Hillerkuss, P. C. Schindler, J. Li, R. Palmer, D. Korn, S. Muehlbrandt, D. Van Thourhout, B. Chen, R. Dinu, M. Sommer, C. Koos, M. Kohl, W. Freude, J. Leuthold, *Nat. Photon.* **2014**, *8*, 229.
[52] A. Melikyan, K. Köhnle, M. Lauermann, R. Palmer, S. Koeber, S. Muehlbrandt, P. C. Schindler, D. L. Elder, S. Wolf, W. Heni, C. Haffner, Y. Fedoryshyn, D. Hillerkuss, M. Sommer, L. R. Dalton, D. Van Thourhout, W. Freude, M. Kohl, J. Leuthold, C. Koos, *Opt. Express* **2015**, *23*, 9938.
[53] C. Haffner, W. Heni, Y. Fedoryshyn, J. Niegemann, A. Melikyan, D. L. Elder, B. Baeuerle, Y. Salamin, A. Josten, U. Koch, C. Hoessbacher, F. Ducry, L. Juchli, A. Emboras, D. Hillerkuss, M. Kohl, L. R. Dalton, C. Hafner, J. Leuthold, *Nat. Photon.* **2015**, *9*, 525.
[54] C. Haffner, W. Heni, Y. Fedoryshyn, J. Niegemann, A. Melikyan, D. L. Elder, B. Baeuerle, Y. Salamin, A. Josten, U. Koch, C. Hoessbacher, F. Ducry, L. Juchli, A. Emboras, D. Hillerkuss, M. Kohl, L. R. Dalton, C. Hafner, J. Leuthold, *Nat. Photon.* **2015**, *9*, 525.
[55] W. Heni, C. Haffner, B. Baeuerle, Y. Fedoryshyn, A. Josten, D. Hillerkuss, J. Niegemann, A. Melikyan, M. Kohl, D. Elder, L. R. Dalton, C. Hafner, J. Leuthold, *J. Lightwave Technol.* **2016**, *34*, 393.
[56] C. Hössbacher, A. Josten, B. Baeuerle, Y. Fedoryshyn, H. Hettrich, Y. Salamin, W. Heni, C. Haffner, C. Kaiser, R. Schmid, D. Elder, D. Hillerkuss, M. Möller, L. R. Dalton, J. Leuthold, *Opt. Express* **2017**, *25*, 1762.
[57] B. Baeuerle, C. Hoessbacher, W. Heni, Y. Fedoryshyn, A. Josten, C. Haffner, T. Watanabe, D. L. Elder, L. R. Dalton, J. Leuthold, in *2018 Optical Fiber Communications Conf. and Exposition (OFC)*, IEEE, Piscataway, NJ **2018**, pp. 1–3.
[58] B. Baeuerle, W. Heni, Y. Fedoryshyn, C. Hoessbacher, U. Koch, A. Josten, T. Watanabe, C. Uhl, H. Hettrich, D. L. Elder, L. R. Dalton, M. Möller, J. Leuthold, in *Optical Fiber Communication Conf.*, Optical Society of America, Washington, DC **2019**, pp. M2F–3.
[59] B. Baeuerle, W. Heni, C. Hoessbacher, Y. Fedoryshyn, U. Koch, A. Josten, T. Watanabe, C. Uhl, H. Hettrich, D. L. Elder, L. R. Dalton, M. Möller, J. Leuthold, *Opt. Express* **2019**, *27*, 16823.
[60] W. Heni, Y. Fedoryshyn, B. Baeuerle, A. Josten, C. Hoessbacher, A. Messner, C. Haffner, Y. Salamin, U. Koch, T. Watanabe, D. L. Elder, L. R. Dalton, J. Leuthold, in *Optical Fiber Communication Conf.*, Optical Society of America, Washington, DC **2019**, pp. Tu2H–4.
[61] M. Ayata, Y. Fedoryshyn, W. Heni, B. Baeuerle, A. Josten, M. Zahner, U. Koch, Y. Salamin, C. Hoessbacher, C. Haffner, D. L. Elder, L. R. Dalton, J. Leuthold, *Science* **2017**, *358*, 630.
[62] A. Messner, P. A. Jud, J. Winiger, W. Heni, B. Baeuerle, M. Eppenberger, U. Koch, C. Haffner, H. Xu, D. L. Elder, L. R. Dalton, P. Ma, J. Leuthold, in *Optical Fiber Communication Conf.*, Optical Society of America, Washington, DC **2020**, pp. M1D–3.
[63] M. Pirola, F. Cappelluti, G. Giarola, G. Ghione, *J. Lightwave Technol.* **2003**, *21*, 2989.
[64] F. Cappelluti, A. Mela, M. Pirola, G. Ghione, in *Microwave Symp. Digest, 2004 IEEE MTT-S Int.*, vol. *2*, IEEE, Piscataway, NJ **2004**, pp. 769–772.
[65] Lumerical Inc., https://www.lumerical.com/products/, **2019**.
[66] Synopsys Inc., *RSoft CAD User Guide, v2019.09*, Synopsys Inc., Ossining, NY, **2019**.
[67] G. Ghione, F. Bertazzi, M. Ghomashi, M. Goano, A. Tibaldi, M. Vallone, in *High Frequency Technologies Workshop*, Huawei, November 2020.
[68] R. Palmer, S. Koeber, D. L. Elder, M. Woessner, W. Heni, D. Korn, M. Lauermann, W. Bogaerts, L. Dalton, W. Freude, J. Leuthold, C. Koos, *J. Lightwave Technol.* **2014**, *32*, 2726.
[69] R. Soref, B. Bennett, *IEEE J. Quantum Electron.* **1987**, *23*, 123.
[70] F. Bertazzi, O. A. Peverini, M. Goano, G. Ghione, R. Orta, R. Tascone, *IEEE Trans. Microwave Theory Tech.* **2002**, *50*, 2108.
[71] F. Bertazzi, G. Ghione, M. Goano, *IEEE Trans. Microwave Theory Tech.* **2003**, *51*, 2029.

[72] A. Tibaldi, M. Ghomashi, F. Bertazzi, M. Goano, M. Vallone, G. Ghione, *Opt. Express* **2020**, *28*, 29253.
[73] B. Chmielak, M. Waldow, C. Matheisen, C. Ripperda, J. Bolten, T. Wahlbrink, M. Nagel, F. Merget, H. Kurz, *Opt. Express* **2011**, *19*, 17212.
[74] P. Dong, L. Chen, Y.-k. Chen, *Opt. Express* **2012**, *20*, 6163.
[75] W. Heni, Y. Kutuvantavida, C. Haffner, H. Zwickel, C. Kieninger, S. Wolf, M. Lauermann, Y. Fedoryshyn, A. F. Tillack, L. E. Johnson, D. L. Elder, B. H. Robinson, W. Freude, C. Koos, J. Leuthold, L. R. Dalton, *ACS Photon.* **2017**, *4*, 1576.
[76] R. Orta, A. Tibaldi, P. Debernardi, *IEEE J. Quantum Electron.* **2016**, *52*, 1.
[77] S. A. Billings, *Nonlinear System Identification: NARMAX Methods in the Time, Frequency, and Spatio-Temporal Domains*, John Wiley & Sons, New York **2013**.
[78] The MathWorks, Inc., *MATLAB and Deep Learning Toolbox Release 2015a*, The MathWorks, Inc., Natick, MA **2015**.

Alberto Tibaldi received the B.Sc., M.Sc., and Ph.D. in electronic engineering from the Polytechnic of Turin, in 2009, 2011, and 2015, respectively. From 2012 to 2019, he was with the Italian National Council of Research (CNR) as a research fellow. Since 2019, he has been with the Department of Electronics and Telecommunications, Polytechnic of Turin, as an assistant professor, where he teaches courses on semiconductor devices and numerical analysis. His scientific interests mainly include the multiphysics modeling of optoelectronic devices.

Mohammmadamin Ghomashi received the B.Sc. in electronic engineering from Shiraz University of Technology in 2013. He received his M.Sc. in microelectronic engineering from Amirkabir University of Technology (Tehran Polytechnic) in 2016. Since 2018, he has been working toward his Ph.D. in Polytechnic of Turin. His research activity is focused on the modeling of electro/optic plasmonic organic hybrid modulators.

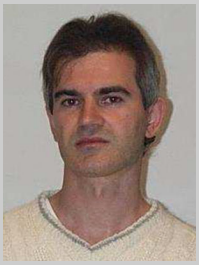

Francesco Bertazzi received the Laurea and Ph.D. in electronics engineering from the Politecnico di Torino, Turin, Italy, in 2000 and 2003, respectively. He was a visiting scholar with the Department of Electrical and Computer Engineering at Boston University, Boston, MA. Since 2008, he has been a professor at the Dipartimento di Elettronica e Telecomunicazioni, Politecnico di Torino. His research activity is focused on nonequilibrium Green's function modeling of carrier transport and recombination processes in infrared photodetectors, light-emitting diodes, and semiconductor lasers. His research interests also include band structure calculations, nonlinear physics-based noise analysis, and electromagnetic modeling of optoelectronic devices.

Michele Goano received his Laurea and Ph.D. in electronic engineering from Politecnico di Torino, Turin, Italy, in 1989 and 1993, respectively. In 1994 and 1994, he was a postdoctoral fellow with the Département de Génie Physique, École Polytechnique de Montréal, Montréal, QC, Canada. He joined the faculty of Politecnico di Torino in 1995. He has been a visiting scholar with the School of Electrical and Computer Engineering, Georgia Institute of Technology, Atlanta, GA, USA, with the Department of Information Technology and Media, Mid-Sweden University, Sundsvall, Sweden, and with the Department of Electrical and Computer Engineering, Boston University, Boston, MA, USA. His current research activity is focused on the simulation of optoelectronic devices based on narrow- and wide-bandgap semiconductor materials.

Marco Vallone received his M.Sc. in physics from the Università di Torino (Italy) and Ph.D. in electronic devices from the Politecnico di Torino (Italy) in 1985 and 2016, respectively. In 1985–2008, he was first with Telecom Italia and then with Avago Technologies, working on testing and modeling of optoelectronic devices. Since 2008, he has held a postdoctoral position at the Politecnico di Torino, where he is currently assistant professor. His current research activity is focused on the simulation of optoelectronic devices based on narrow- and wide-bandgap semiconductor materials and on the description of inter- and intraband quantum scattering processes.

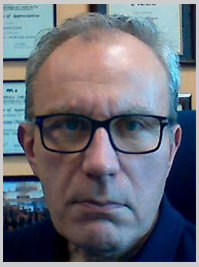

Giovanni Ghione graduated in electronic engineering from Politecnico di Torino in 1981. Since 1990, he has been a full professor in electronics, from 1991 again with Politecnico di Torino. His research has concerned the high-frequency electronics and optoelectronics, including the physics-based modeling of compound semiconductor materials and devices, the design of microwave integrated circuits, the modeling of far infrared (FIR) and NIR photodetectors and electro-optic and electroabsorption modulators. He chaired (2010–2015) the IEEE Electron Devices Society Committee on Compound Semiconductor Devices and Circuits. He was (2016–2021) the Editor in Chief of the IEEE Transactions on Electron Devices.